










# Passive Seismology: Lightweight and Rapid Detection of Arctic Subsea and Sub-Aquatic Permafrost

**Special Collection:**  
The Arctic: An AGU Joint  
Special Collection

Michael Angelopoulos<sup>1</sup> , Trond Ryberg<sup>2</sup> , Christian Frigaard Rasmussen<sup>1</sup>,  
Christian Haberland<sup>2</sup> , Bennet Juhs<sup>1</sup> , Scott Dallimore<sup>3</sup> , Julia Boike<sup>1,4</sup> , and  
Pier Paul Overduin<sup>1</sup> 

<sup>1</sup>Permafrost Research Section, Alfred Wegener Institute Helmholtz Centre for Polar and Marine Research, Potsdam, Germany, <sup>2</sup>Section Geophysical Imaging, GFZ German Research Centre for Geosciences, Potsdam, Germany, <sup>3</sup>Geological Survey of Canada, Natural Resources Canada, Sidney, BC, Canada, <sup>4</sup>Geography Department, Humboldt-Universität zu Berlin, Berlin, Germany

### Key Points:

- We present passive seismic data from Arctic lake, river, lagoon, and subsea permafrost settings
- We applied the maximum H/V amplitude and shortest path to connect H/V peaks and interpret subsurface shear wave velocity contrasts
- Passive seismic H/V ratio measurements of just a few minutes of recording time can be used to investigate the depth of submerged permafrost

### Supporting Information:

Supporting Information may be found in the online version of this article.

### Correspondence to:

M. Angelopoulos,  
[michael.angelopoulos@awi.de](mailto:michael.angelopoulos@awi.de)

### Citation:

Angelopoulos, M., Ryberg, T., Rasmussen, C. F., Haberland, C., Juhs, B., Dallimore, S., et al. (2024). Passive seismology: Lightweight and rapid detection of Arctic subsea and sub-aquatic permafrost. *Journal of Geophysical Research: Earth Surface*, 129, e2023JF007290. <https://doi.org/10.1029/2023JF007290>

Received 8 JUN 2023  
Accepted 23 MAY 2024

**Abstract** Low sea levels during the last Ice Age exposed millions of square kilometers of Arctic shelves which have been subsequently submerged, creating subsea permafrost. In onshore settings, permafrost can also exist beneath water bodies such as coastal lagoons, rivers, and thermokarst lakes. We explored passive seismology as a method for mapping unfrozen sediment thickness above subsea and sub-aquatic permafrost. We present passive seismic data collected with the Mobile Ocean Bottom Seismic Instrument (MOBSI) from the Beaufort Sea near Tuktoyaktuk in Canada, Ivashkina Lagoon on the Bykovsky Peninsula, as well as a lake and river in the Lena Delta, Siberia, Russia. We use borehole data and frost probe measurements to identify permafrost-related H/V measurement peaks and calibrate shear wave velocities for frequency-to-depth conversion. We employ the shortest path and maximum signal amplitude to connect peaks and generate geological profiles. The MOBSI detected the ice-bonded permafrost table beneath the Beaufort Sea, as well as beneath a Siberian lake and lagoon. At Tuktoyaktuk, an ocean bottom seismometer revealed a 5% scatter about the peak frequency for three-minute time windows and over 8 hr of recording time. With peak frequencies ranging from  $4.9 \pm 0.2$  Hz to  $27.6 \pm 1.4$  Hz, the depth to subsea permafrost ranged from  $1.4 \pm 0.1$  m bsl at the shoreline to  $14.0 \pm 0.4$  m bsl 240 m offshore. Given an accurate shear wave velocity, our findings highlight that MOBSI deployment times as short as 3 min are adequate for detecting Arctic subsea and sub-aquatic permafrost.

**Plain Language Summary** During the Ice Age, low sea levels exposed large areas of the Arctic, creating perennially frozen ground known as permafrost. When sea levels rose, this permafrost became submerged. Permafrost can also exist under bodies of water like coastal lagoons, rivers, and lakes. However, we have limited direct measurements of its characteristics and how it is changing over time. To address this, we used a technique called passive seismology to map the thickness of unfrozen sediment above subsea and sub-aquatic permafrost. We collected passive seismic data using the Mobile Ocean Bottom Seismic Instrument (MOBSI) in the Beaufort Sea near Tuktoyaktuk in Canada, Ivashkina Lagoon on the Bykovsky Peninsula, and a lake and river in the Lena Delta, Siberia, Russia. This method involves recording ambient seismic noise to identify differences in the speed of shear waves in the subsurface. These boundaries with contrasting velocities are associated with geological interfaces like the top of permafrost. We used data from boreholes and frost probe measurements to calibrate and verify our passive seismic results.

## 1. Introduction

Permafrost is perennially cryotic ( $<0^\circ\text{C}$ ) earth material. We define permafrost beneath shallow shelf seas as *subsea permafrost*, whereas we use the term *sub-aquatic permafrost* for permafrost beneath lagoons, rivers, and lakes. Beneath shallow shelf seas and lagoons, permafrost is not necessarily frozen because salts in the sediment pore space lower the freezing point of porewater. The freezing point for Arctic shelf sediments with a salinity of 30 ppt is  $-1.8^\circ\text{C}$ , but in lagoon sediments, the freezing point dips even lower when high amounts of salt concentrate beneath the lagoon ice cover (Angelopoulos, Overduin, Westermann, et al., 2020). Offshore, inundation has warmed the top of permafrost by  $10\text{--}15^\circ\text{C}$  since the last transgression (Overduin et al., 2019). Thermokarst lakes, which have average annual bottom water temperatures of  $2.7^\circ\text{C}\text{--}4.0^\circ\text{C}$  in northeastern Siberia (Boike, Georgi, et al., 2015), also warm and thaw permafrost. As the variability of ice bonding of sub-aquatic permafrost greatly affects shear strength and other physical properties, mapping its distribution can be critical for a variety of engineering considerations

© 2024. The Author(s).  
This is an open access article under the terms of the [Creative Commons Attribution License](https://creativecommons.org/licenses/by/4.0/), which permits use, distribution and reproduction in any medium, provided the original work is properly cited.

including foundations for subsea structures and coastal erosion. However, a particularly important consideration relates to organic carbon storage, mobilization, and its potential release to the atmosphere. A substantial reservoir of organic carbon (Miesner et al., 2023) and methane gas hydrates (Riedel et al., 2017; Ruppel, 2015; Stocker et al., 2014) exists within and beneath thick occurrences of subsea permafrost, which if destabilized and released, may contribute to climate warming (Ruppel & Kessler, 2017). The state-of-the-art subsea permafrost model of the northern hemisphere shows that 97% of subsea permafrost is in disequilibrium and is thawing at its lower boundary (Overduin et al., 2019). Top-down thaw rates depend on many factors, including water temperature, salt transport into the sediment, and bottom-fast ice occurrence. However, since considerably less research has been carried out on subsea permafrost compared to terrestrial permafrost (Angelopoulos, Overduin, Miesner, et al., 2020), there is a lack of observational data regarding its morphology and degradation (or aggradation) rate. Geophysical instruments are useful tools to close this knowledge gap, but not all emergent techniques have been tested yet. In this study, we explore the use of passive seismic technology in multiple subsea and sub-aquatic permafrost settings and demonstrate its ability to reveal the thickness of unfrozen sediment above frozen subsea or sub-aquatic permafrost.

Geotechnical drilling and thermistor chains have traditionally been the go-to exploratory tool both for investigations of terrestrial and sub-aquatic permafrost (e.g., Kurfurst & Dallimore, 1991). With water jet drilling, sediment cannot be extracted, but temperature cables can be still be installed. Drilling is a costly and difficult endeavor, especially in the remote Arctic. Over the past few decades, geophysical methods have matured and have been increasingly deployed to map permafrost and ground ice characteristics (Hauck, 2013). In water-covered areas, electrical resistivity tomography (ERT) may consist of surveys with underwater (submerged), suspended, or floating electrodes (Loke & Lane, 2004). To map permafrost, electrical resistivity tomography (ERT) relies on the strong resistivity contrast between water-saturated unfrozen sediment (seasonally thawed layer or talik) and ice-saturated frozen ground. Offshore, ERT typically uses a floating electrode streamer behind a boat (Angelopoulos et al., 2019, 2021; Overduin et al., 2012; Pedrazas et al., 2020). A recent global inversion study by Arboleda-Zapata et al. (2022) showed that incorporating water layer resistivity and thickness into the inversion of raw ERT data is crucial to reduce the uncertainty of ice-bearing permafrost table depth estimation. Electromagnetic methods operated at low frequencies offer the capability to quantify sub-aquatic ice-bearing permafrost thickness (Sherman et al., 2017), but at a lower vertical resolution compared to ERT surveys. For underwater surveys, ground-penetrating radar (GPR) is limited to freshwater environments, because radar signals are strongly absorbed by saltwater. Hence, GPR is particularly effective at mapping frozen/unfrozen horizons in sediment beneath bottom-fast ice in freshwater areas (Stevens et al., 2009).

Seismic refraction or reflection surveying have become the main geophysical tool for investigations of subsea permafrost because primary (P)- and shear (S)-waves propagate more rapidly in frozen sediment (Scott et al., 1978). In fact, the seismically delineated permafrost extents in the American Beaufort Sea (Brothers et al., 2016) and Kara Sea (Rekant & Vasiliev, 2011) align closely with the modeled subsea permafrost extent (Overduin et al., 2019). Building off the work of Riedel et al. (2017), seismic reflection data has been used to map the top and base of subsea permafrost on the Canadian Beaufort Shelf, as well as the bottom of the gas hydrate stability zone (Grob et al., 2023). The nature of the reflections is evident through their polarity and orientation with respect to the seabed. Forward modeling studies of two-dimensional reflection seismic data show that multiples from the seafloor and the permafrost table can mask the bottom of subsea permafrost, especially for non-dipping interfaces and thin permafrost (<50 m) (Duchesne et al., 2023). Though effective, active seismic surveying carries an environmental pollution risk. The main pollutant is the acoustic noise from the seismic sources, which can impact marine life (Blackwell et al., 2015; McCauley et al., 2017). Passive seismology, which relies on ambient seismic noise, is pollution-free, has a low environmental impact and is an emerging tool for permafrost studies. The technique uses the horizontal (H)/vertical (V) spectral ratio of ambient seismic noise at different frequencies (i.e., H/V method) to identify shear wave velocity contrasts and has been applied in subsea permafrost areas (Krylov et al., 2022; Overduin, Haberland, et al., 2015). Corroborated by soil temperature and electrical resistivity data, a 1-year passive seismic time-series on land revealed that the near-surface H/V ratio is seasonally dependent (Kula et al., 2018). Although the method can be effective at monitoring seasonal active layer changes, careful attention must be given to excluding non-geological effects on the H/V ratio for high frequencies (Köhler & Weidle, 2019). Time-lapse passive seismic data is also effective at monitoring the degradation of the permafrost table, as revealed by a controlled heating experiment (Cheng et al., 2022).

Ambient seismic noise originates from human and natural sources, including ocean waves, atmospheric disturbance, and tectonic activity. S-waves travel slower than P-waves and the particles passing through them oscillate

perpendicular to the direction of wave propagation. When the S-wave frequency matches the natural oscillation frequency of a subsurface material, the structure resonates and produces a local amplification of the seismic signal (Lunedei & Malischewsky, 2015). For a horizontally layered medium and two-layer system, the thickness of the uppermost layer is inversely proportional to the fundamental peak resonance frequency. We hypothesize that passive seismology and the H/V method can be used in multiple Arctic subsea and sub-aquatic permafrost settings, because the shear wave velocity contrast at unfrozen sediment/frozen sediment interfaces is sufficiently large to generate peaks in H/V ratio versus frequency curves. We test this hypothesis by carrying out passive seismic surveys at Arctic water bodies containing frost probe or borehole records of the ice-bonded permafrost table (IBPT). Building off the pioneering work of Overduin, Haberland, et al. (2015) near Muostakh Island in the Laptev Sea, our study includes subsea permafrost beneath the Canadian Beaufort Sea, a lagoon at the coast of the Laptev Sea, as well as a river and lake in the Lena Delta, Russia. Our objectives are to (a) collect an Arctic passive seismic data set for sites located in various types of water bodies (freshwater and saltwater) and water depth associated with floating ice and bottom-fast ice conditions in winter; (b) employ a standardized method for the analysis of H/V signals; (c) use shortest path and maximum amplitude techniques to interpret H/V signal peaks and sediment interfaces; and (d) validate our interpretations with borehole data and frost probe measurements. We aim to provide new insights on how the site conditions and data processing strategy influence our capability to reveal permafrost underwater.

## 2. Field Sites

We investigated sub-aquatic permafrost beneath an Arctic lake, river, and lagoon in northeastern Siberia, as well as subsea permafrost offshore of Tuktoyaktuk in the Canadian Arctic. Banja Lake is situated east of Research Station Samoylov Island in the Lena Delta (Figure 1c). The lake is 400 m long and 130 m wide and unlike typical thermokarst lakes, it is ovally shaped and seasonally connected to the Lena River through a channel during spring freshet. This suggests that the lake is most likely a remnant of a river channel (oxbow lake) (Chetverova et al., 2018). Approximately 1.5 km northwest of Banja Lake is the Lena River (Samoylov Island) site (Figure 1b). Primarily underlain by Yedoma silts, the river channel in this area formed 2000–4000 years ago (Schwamborn et al., 2002). The Lena River (Chay-Tumus) site (Figure 1a) lies 23 km to the west of the Lena River (Samoylov Island) profile in the Olenyokskaya Channel. The Olenyokskaya Channel is 200 km long, developed after Yedoma sediment deposition (Schirrmeister et al., 2003), and is underlain by bedrock (Are & Reimnitz, 2000) (Figure 1d).

Ivashkina Lagoon is on the southern coastline of the Bykovsky Peninsula southeast of the Lena Delta (Figure 2b), where thermokarst processes have a significant impact on the landscape (Grosse et al., 2005, 2008). The Yedoma deposits are organic-rich and contain volumetric ice contents as high as 80%–90% (Grosse et al., 2007; Günther et al., 2015; Schirrmeister et al., 2018; Siegert et al., 2002). Toward the lagoon's northern shoreline, the IBPT was 15.1 m below sea level (bsl) in 2014 (Ulyantsev et al., 2016). In the lagoon center, which intersects the passive seismic profile, Sapart et al. (2017) reported an IBPT depth of 11.4 m bsl. The lagoon fills a drained lake basin (Schirrmeister et al., 2018), but thermo-erosional widening of the shoreline is occurring at rates greater than 0.5 m/year along the lagoon's western edge (Schirrmeister et al., 2018).

Tuktoyaktuk Island is in northwestern Canada near the hamlet of Tuktoyaktuk (Figure 2a). The island is highly vulnerable to coastal erosion due to its exposure to the Beaufort Sea and because the coastal sediments consist of glaciofluvial deposits overlying massive ground ice (Murton, 2001; Wolfe et al., 1998). As revealed by geophysical well logs, subsea permafrost is prevalent in the Canadian Beaufort Sea (Hu et al., 2013). The warm summer discharge from the Mackenzie River exerts a major control on the IBPT degradation rate nearshore (Taylor et al., 2013) and submerged thermokarst depressions result in IBPT depths of almost 100 m for inundation times on the order of 5000 years (Taylor et al., 1996). In this study, we present passive seismic data from the northern shoreline of Tuktoyaktuk Island. It is the only site where we have a precise account of the inundation time at each sounding, allowing us to infer the IBPT degradation rate. From 1947 to 2018, the mean erosion rate along the northwestern shoreline was  $1.63 \pm 0.04$  m/year (Whalen et al., 2022).

## 3. Methods

### 3.1. Instrumentation and Data Collection

We carried out passive seismic surveys during summer campaigns in northeastern Siberia in 2016 (Morgenstern et al., 2017) and northwestern Canada in 2018 (Boike & Dallimore, 2019). We collected the data using the Mobile



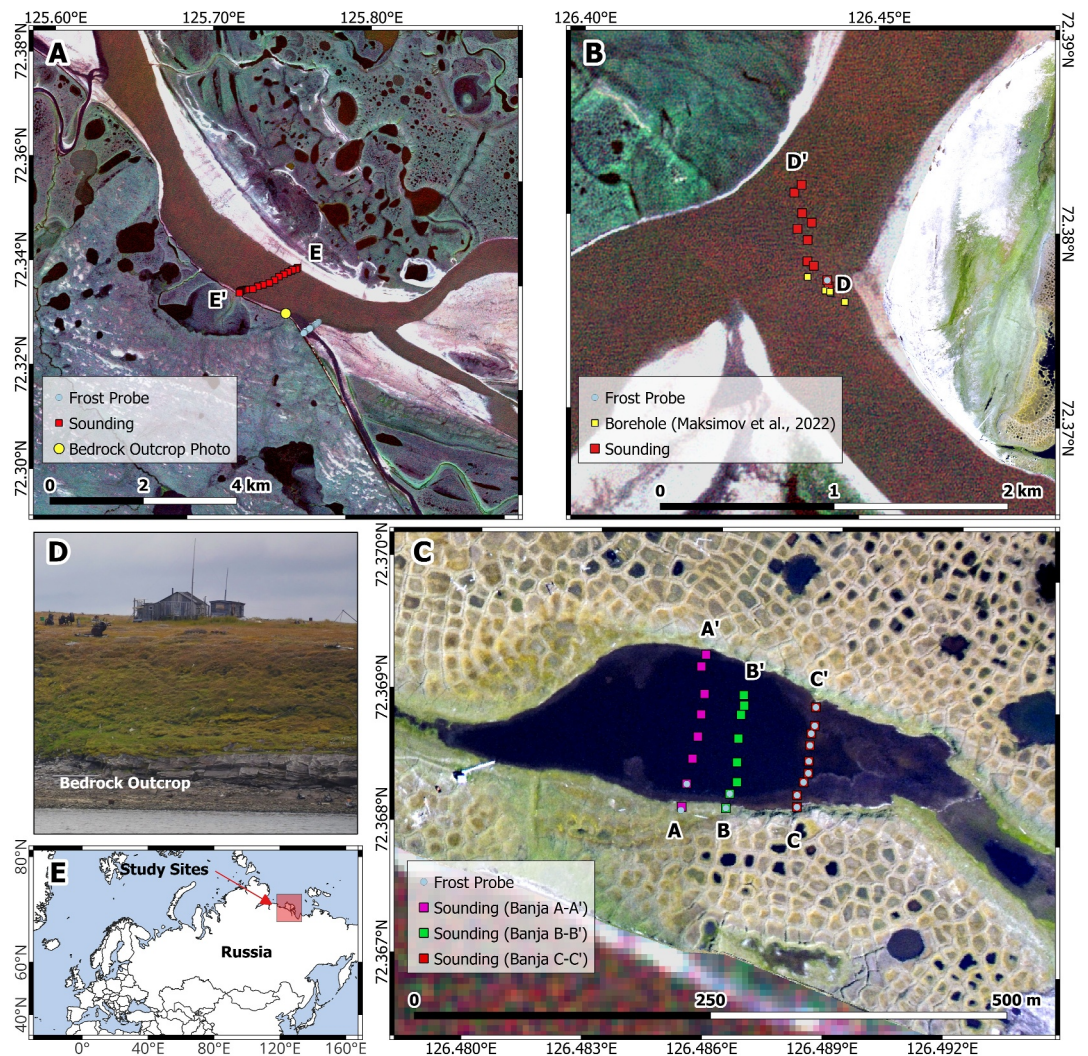


**Figure 1.** Sub-aquatic passive seismic soundings (red, green, or magenta squares) carried out on the Olenyokskaya Channel in the Lena River at Chay-Tumus (panel a), the Lena River near Samoylov Island (panel b), and Banja Lake (panel c). The individual soundings were calibrated using data from frost probes (depicted as blue circles) and boreholes (represented by yellow squares), providing precise measurements of the depth to sub-aquatic permafrost. At Chay-Tumus, the riverbank clearly exposes bedrock (panel d), which may be shallower than the permafrost table beneath the riverbed. All three sites are located in the Lena Delta, as illustrated in panel (e). The background images are a RapidEye image from 25 August 2015 (panels a and b) and an orthomosaic image from Boike, Veh, et al. (2015) (panel c).

Ocean Bottom Seismic Instrument (MOBSI) developed by the German Research Centre for Geosciences (GFZ). The MOBSI is portable (9 kg) and consists of a water tight, heavy-duty pressure housing (diameter 30 cm, height 35 cm) containing a three-component broadband sensor. There are three channels (two horizontal and one vertical) recorded by the built-in data logger to monitor ambient seismic noise. Ryberg et al. (2020) provide a summary of the device's technical specifications.

For all soundings, the sampling frequency was set to 100 samples per second, and the sensor recorded ambient seismic noise for a few to several minutes at each location. The specific deployment time for each sounding is available in the online data publication. Deployed by a steel cable from a small boat or zodiac, the device was lowered to the bottom of the water bodies or top of the beach area (Figure 2d). The overlying water column (freshwater or saltwater) does not have any impact on H/V data interpretation when the water depths are less than 100 m (Overduin, Haberland, et al., 2015). The steel cable was outfitted with a communications cable, which allowed for live data analysis and quality control via a shipboard monitor. This insured that the tilt of the instrument was correct (less than 5°) and that the deployment time was sufficient. We stopped data collection until

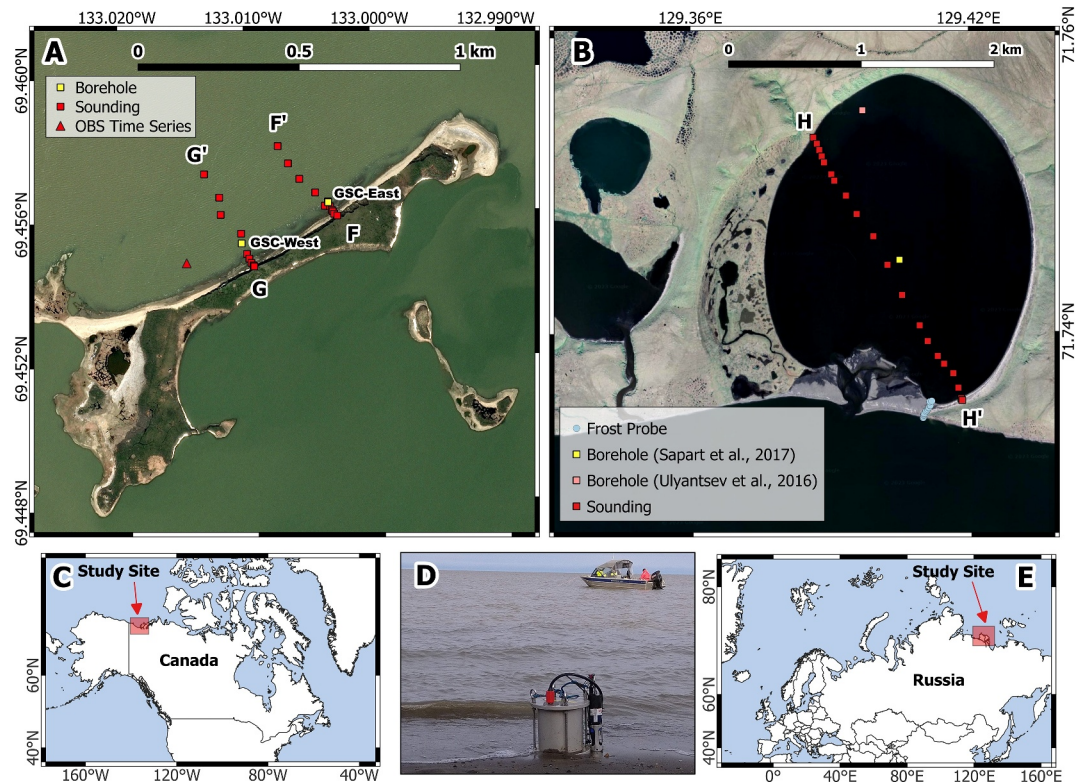


**Figure 2.** Subsea and sub-lagoon passive seismic soundings carried out offshore of Tuktoyaktuk Island (panel a) and Ivashkina Lagoon (panel b). The individual soundings were calibrated using data from boreholes (represented by yellow squares), providing precise measurements of the depth to ice-bonded permafrost. On Tuktoyaktuk Island, an ocean bottom seismometer (OBS) (red triangle) was deployed for 8 hr to monitor peak frequency stability. Tuktoyaktuk Island is positioned in the Canadian Beaufort Sea, as indicated in panel (c). An example of the Mobile Ocean Bottom Seismometer Instrument (MOBSI) deployed on the beach of Tuktoyaktuk Island is depicted in panel (d). Ivashkina Lagoon is situated on the southern coastline of the Bykovsky Peninsula in Siberia, just southeast of the Lena Delta (panel e). The background images are a Microsoft Bing map (panel a) and a WorldView-3 image from 2 September 2016 © Digital Globe (panel b).

the real-time H/V ratio stabilized, that is, not changing with time. The MOBSI data was recorded in an internal RAW format that was converted to miniSEED format. Information regarding data format and conversion are available in Lendl (2021).

To demonstrate the temporal evolution and/or stability of the H/V ratio measurements, we analyzed seismic data from ocean bottom seismometer (OBS) noise recordings in the Tuktoyaktuk study area from 2021 (for position, see Figure 2a). The technical specifications of the OBS are reported in Ryberg et al. (2022). Although not co-located with one of our H/V measurements with the MOBSI in 2018, the long duration of the OBS deployment allows us to evaluate the H/V peak stability and to estimate its uncertainty (refer to Figure 5). Hence, the short MOBSI deployment time of only a few to several minutes can be assessed.

### 3.2. Data Processing

#### 3.2.1. Power Spectra

To calculate the power spectral density (PSD), we used the signal processing toolbox in MATLAB and applied a fast Fourier transform (FFT) to convert from the time domain to the frequency domain. We used the entire time window for the PSD calculation. To smooth the PSD versus frequency curves for each channel ( $H_1$ ,  $H_2$ , and V), we applied the Konno-Ohmachi method (Konno & Ohmachi, 1998), also available in MATLAB (<https://www.mathworks.com/matlabcentral/fileexchange/68205-konno-ohmachi-smoothing-function-for-ground-motion-spectra>). The smoothing parameter ( $s$ ) is inversely correlated with the size of the smoothing window and so a



**Table 1**  
*Calibrated Shear Wave Velocities*

Site	Unfrozen sediment thickness (m)	Peak frequency (Hz)	Inferred velocity (m/s)
Banja Lake (B-B')	2.7	5.1	56
Lena River (D-D')	1.96	11.4	89
Ivashkina Lagoon (H-H')	8.6	6.2	212
Tuktoyaktuk (F-F')	1.9	20.3	154

lower value results in smoother spectra. In our analyses, we select a value of 40 as a default, but also show results for 20 and 10 for Ivashkina Lagoon. The smoothing factor is important, because it affects the complexity of the spectra, that is, the number of spectral peaks. Following data smoothing, we calculated the spectral H/V (Horizontal over Vertical) ratio using Equation 1.

$$\frac{H}{V} = \frac{\sqrt{PSD(H_1) + PSD(H_2)}}{\sqrt{PSD(V)}} \quad (1)$$

At this stage, peak candidates representing a possible geological interface were displayed. The frequency ( $f_0$ ) of a peak candidate is related to the depth ( $d$ ) of the geological interface as a function of the shear wave velocity ( $v_s$ ) as shown in Equation 2. As first demonstrated by Ibs-von Seht and Wohlenberg (1999), there is a correlation between the peak frequency and the soft-layer sediment thickness above bedrock for a two-layer system. Overduin, Haberland, et al. (2015) then showed that this principle also applies to determining the unfrozen sediment layer thickness above ice-bonded subsea permafrost.

$$d = \frac{v_s}{4f_0} \quad (2)$$

Prior to peak selection, we applied an upper frequency cutoff of 40 Hz and lower frequency cutoff of 2 Hz to the data for water depths greater than 0.5 m. For water depths shallower than 0.5 m, the lower frequency filter was adjusted to 5 Hz. For shallow water depths, bottom-fast ice is present for a large fraction of the freezing season and this tends to preserve sub-aquatic and subsea permafrost. The frequency cutoffs were applied to remove high and low frequency noise and simplify the peak selection process. For the shear wave velocity range in this study (56–212 m/s), an upper frequency cutoff of 40 Hz corresponds to a depth range of 0.34 m (Banja Lake) to 1.33 m (Ivashkina Lagoon) below the sediment surface. The peaks associated with frequencies above 40 Hz do not represent the IBPT and are therefore not considered in the peak frequency analysis. In Overduin, Haberland, et al. (2015), the lower frequency cutoff was set to 0.5 Hz because of the low-frequency limitation associated with the limited noise recording time (30-min time windows) (Overduin, Haberland, et al., 2015). In this paper, the lower frequency cutoff was set to 2.0 Hz because the measurement time was on the order of a few to several minutes. According to SESAME guidelines (Acerra et al., 2004), the recommended recording duration for a minimum expected peak frequency of 2 Hz is 5 min. For a minimum peak frequency of 5 Hz, the recommended recording time is 3 min. Every sounding that is compared to a borehole or frost probe measurement for validation contains a peak frequency above 5 Hz and a deployment time greater than 3 min.

### 3.2.2. Shear Wave Velocity Determination

The peaks for velocity calibration were manually picked for the soundings intersecting the borehole or frost probe locations. For these soundings, we selected the greatest peak height or amplitude. Using Equation 2, the shear wave velocity was derived from the borehole- or frost probe-determined unfrozen/frozen sediment interface depth (below sediment surface) and the fundamental peak frequency. The inferred shear wave velocities are summarized in Table 1.

As MOBSI was submerged, all interface depths in Table 1 are referenced to the water/sediment interface. In the case of Banja Lake, the deepest IBPT among the three profiles was utilized for velocity calibration. Following the assumptions of the H/V method, one propagation velocity was used consistently within each profile. For the Lena

River (Samoylov Island) profile, we used a frost probe measurement that intersected the start of the profile (Morgenstern et al., 2017). Further borehole studies suggest that this was a seasonally frozen layer that had not completely thawed out yet (Maksimov et al., 2022). For the Lena River (Chay-Tumus), there was a lack of validation or calibration data at the sounding locations. Consequently, the velocity derived for the Lena River (Samoylov Island) profile was applied in this context. At Ivashkina Lagoon, we opted for the borehole IBPT reported by Sapart et al. (2017), as it is closest to the profile center. In the case of Tuktoyaktuk, where a borehole (GSC-East) (Boike & Dallimore, 2019) nearly intersects a sounding, we utilized this calibrated velocity for both profiles.

### 3.2.3. Peak Selection

We used the find peaks function (<https://www.mathworks.com/help/signal/ref/findpeaks.html>) in MATLAB to locate peaks in the H/V ratio versus frequency curves in linear space. The function returns the frequency, H/V ratio (peak height or amplitude), prominence, and width of the peaks. The peak prominence refers to the local peak height, meaning that we calculate the difference between the peak height and the base level. The base level is defined as the minimum H/V ratio over a specified frequency range. This range is determined as follows: extend a horizontal line from the left and right of peak until it either, (a) intersects a part of the signal with a greater height, or (b) reaches the left or right limits of the filtered bandwidth. Since there are usually many peaks, we used the following criteria (Equation 3) to determine if a peak is significant and thus a candidate for a geological interface (Pontrelli, 2019). For this criterion, we assumed a frequency-dependent normal distribution of the H/V ratio and that the difference between the peak height and the peak prominence should be smaller than the peak height divided by the square root of two. In the absence of strong peaks, energy is distributed across the frequency range, which results in a decrease of the peak prominence.

$$(\text{peak}_{\text{height}} - \text{peak}_{\text{prominence}}) < \frac{\text{peak}_{\text{height}}}{\sqrt{2}} \quad (3)$$

Once all the significant peaks were assembled, we calculated the shortest path out of all possible paths through the peaks (nodes) based on the assumption that an IBPT is gently varying along the profiles. To accomplish this task, we used the shortest path tree function (<https://www.mathworks.com/help/matlab/ref/graph.shortestpathtree.html>) in MATLAB. It is important to note that this shortest path algorithm differs from a pure lateral constraint method. While the latter seeks the shortest distance between neighboring soundings and forms an aggregate, it exhibits a directional bias. In contrast, the shortest path technique produces consistent results regardless of the starting node. As inputs to the function, the possible node pair connections are defined and each node pair (sounding to sounding) is weighted by real-world distance. Since MOBSI was submerged, water depth is accounted for in the shortest path. The paths are restricted to one node per sounding (i.e., a shortest path cannot pass through more than one node for the same sounding). Additional constraints are present for soundings that intersect borehole or frost probe measurements. For these soundings, we pick the candidate peak (frequency converted to depth) closest to the known IBPT depth. We employ the shortest path to create a 2D IBPT profile, because the prevailing assumption is that the IBPT should be a smooth and sloping feature in the case of subsea permafrost or a smooth and bowl-shaped feature in the case of lake cross-sections. As a comparison, we also show 2D IBPT profiles produced by picking the maximum amplitude (or peak height) for each sounding.

Due to the relatively short noise recording time of the MOBSI device, it is difficult to evaluate the uncertainty of the peak determination method and the resulting depths to geological interfaces, including the subsea and sub-aquatic IBPT. Data from longer duration experiments in the Lena Delta (Overduin, Haberland, et al., 2015) suggests a peak frequency uncertainty of several percent. However, the latter is fairly stable compared to the peak height of the H/V ratios at the peak frequency. The major unknown when converting the peak frequency to depth of the IBPT is the S-wave velocity of the overlying unfrozen material. In this paper, we calibrate this velocity by comparing the peak frequency with a manually determined IBPT by using borehole data or frost probe measurements, thus deriving an estimate of that velocity locally. Furthermore we used this velocity for all H/V results at the specific site/profile for depth conversion of the frequency peaks where there were no direct measurements. We are fully aware that the assumption of a homogeneous sedimentary velocity along the studied profiles might not be valid. In this sense, the derived IBPT depths should be treated as *model depth*. Since the data sets do not

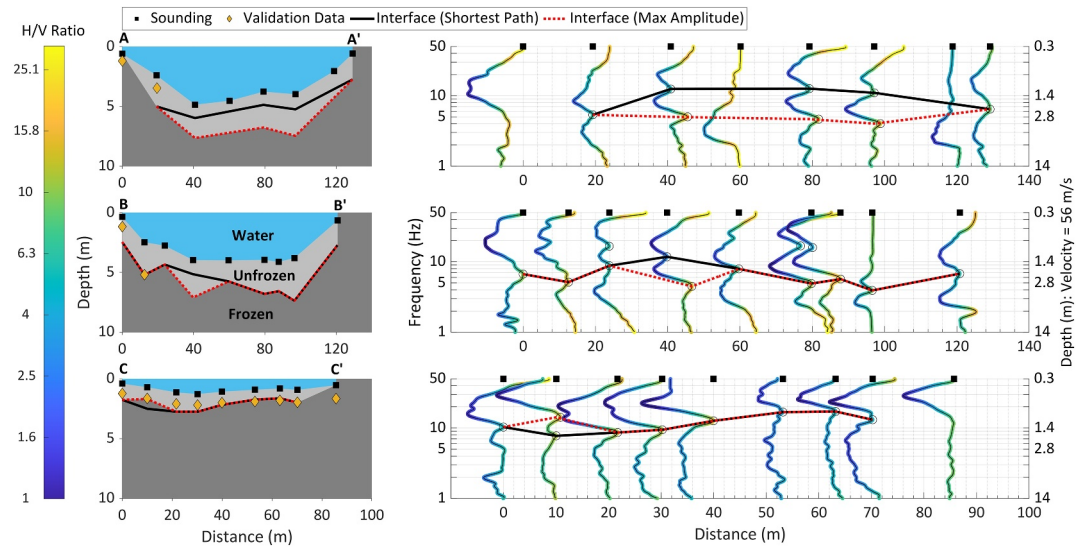


**Figure 3.** Passive seismic findings regarding sub-aquatic permafrost at Banja Lake are depicted. In the right column, H/V measurements are displayed on the distance axis at each sounding position. To achieve this, the logarithm of the H/V ratios was multiplied by a survey-length dependent factor and added to the profile distance. The sounding position is aligned with the significant peak (if present), determined by the shortest path algorithm. In cases where no peak is present, the sounding position aligns with the H/V measurement at 50 Hz. Significant peaks within the 2–40 Hz range for each sounding are denoted as black circles. The potential ice-bonded permafrost boundaries are delineated by the shortest path through the peaks (depicted as the black line) and the maximum peak amplitudes (illustrated as a dotted red line). The shortest path accounts for the water depth at each sounding. The left column displays interpreted results, depicting the water layer, unfrozen ground, and frozen ground.

contain MOBSI measurements at two stations simultaneously, an estimation of shear wave velocity from the dispersion of surface waves was not performed.

## 4. Results

We detected frozen permafrost beneath freshwater lakes and saltwater bodies (lagoons and seas) for peak frequencies ranging from approximately 4–30 Hz. We present the H/V ratio peaks between 2 and 40 Hz for all profiles, but the complete H/V ratio spectra between 1 and 50 Hz. To facilitate the visualization of H/V ratios in 2D profiles, the H/V ratios (in log form) are multiplied by survey-length dependent factors and plotted versus frequency on the distance axis, along with the sounding positions. The curves are color-coded with log-scaled H/V ratios between 1 and 30 to enhance visualization. Given the lack of compelling evidence supporting the detection of the sub-aquatic permafrost layer beneath the Lena River by the MOBSI, the results of these profiles are provided in Figure S1. Section 5.3 presents the reasons behind this, including a brief discussion on the necessity for alternative geophysical data sets.

### 4.1. Sub-Lake Permafrost

In profiles A-A' and B-B' (Figure 3) at Banja Lake, the MOBSI data reveals the presence of two distinct geological contacts within the upper 3 m of sediment. The shallower structure, found at sediment depths less than 1.4 m (peak frequencies >10 Hz), exhibits weaker H/V ratios compared to the deeper structure. This deeper unit, characterized by higher amplitude peaks, extends to a maximum depth of 3 m below the lake bed (peak frequency of 4 Hz) and nearly 8 m below the water level. Given that these peaks serve as indicators of subsurface structure, the shortest path algorithm delineates the shallower structure, whereas the maximum amplitudes describe the deeper structure. In profile A-A', the deeper structure appears more plausible for representing the permafrost table. Similarly, in profile B-B', the shortest path follows the strongest amplitude peaks of the deeper unit, with the exception of only one sounding. The overall shape and thaw depth of the permafrost table seem realistic if permafrost degradation is recent. Notably, the mean H/V ratio for the shortest path peaks is 10.3 for profile B-B' compared to 7.3 for profile A-A', suggesting once again that the deeper unit exhibits a stronger shear wave



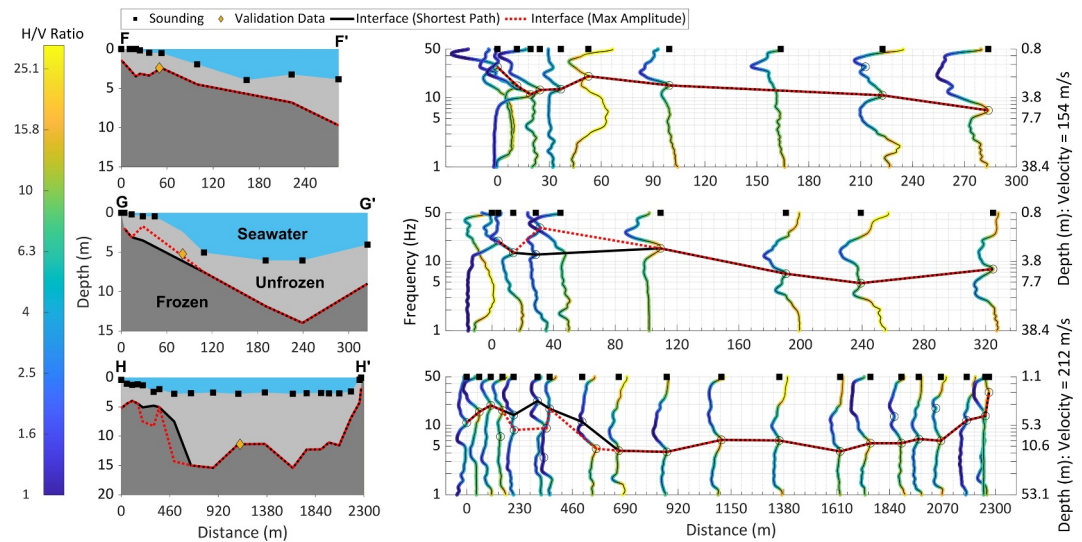


**Figure 4.** Passive seismic findings regarding subsea permafrost at Tuktoyaktuk (F-F', G-G') and sub-lagoon permafrost at Ivashkina Lagoon (H-H'). Refer to the caption in Figure 3 for an explanation of how the H/V measurements are presented and interpreted.

velocity contrast compared to the shallower interface. In profile C-C' (Figure 3), there is typically only one peak candidate at each location, except for the second sounding (which shows two significant peaks) and the ninth sounding (with no peaks). Consequently, the shortest path traverses through the most prominent peaks, except for the second sounding, which has a maximum H/V ratio of 13.7. This profile depicts a single geological interface, with its depth closely aligning with frost probe measurements. Toward the southern end of the profile, the depths determined by the shortest path algorithm overestimate the frost probe depths by a factor of 2. This discrepancy arises because the shortest path algorithm selects the deeper and lower amplitude peak, which is not associated with permafrost. The mean and standard deviation of the frost probe depths were  $0.97 \pm 0.09$  m, indicating little variation in seasonal thaw depths below bottom-fast ice zones.

#### 4.2. Sub-Lagoon and Subsea Permafrost

At Ivashkina Lagoon (H-H'), the shortest path generates a distinctive bowl-shaped interface, characteristic of a talik shape beneath a water body sitting atop permafrost (Figure 4). Among the 20 soundings, eight feature two significant peaks, while the remaining 12 exhibit only one peak. Soundings with multiple peaks tend to occur at the edges of the profile. Toward the northeast end of the profile, the interface generated by maximum amplitudes reveals a deeper and more undulating IBPT. The maximum depth of the contact reaches 15 m bsl near the lagoon's center for a peak frequency of 4 Hz. The mean H/V ratio for the interface peaks produced by the shortest path is 11.1, consistent with the mean H/V ratios of permafrost-associated interface peaks for Banja Lake. Offshore of Tuktoyaktuk, the interface generated by the shortest path displays similar patterns for both profiles (Figure 4). The interface dips along the beach toward the waterline, presumably due to occasional submergence by high tides and storm surges. Starting at the water's edge, the interface remains stable for shallow water depths (<1 m) where bottom-fast ice forms in winter. In deeper water, the interface depth and overlying layer thickness increase with distance offshore. However, there is a deviation from this pattern at the furthest offshore sounding of G-G', where the interface depth decreases relative to the previous sounding closer to the coastline. The mean H/V ratios of the interface peaks (produced by the shortest path) for Tuktoyaktuk profiles F-F' and G-G' are 14.5 and 12.5, respectively.

#### 4.3. Ocean-Bottom Seismometer

To study the temporal evolution and/or stability of the H/V measurements we analyzed seismic data from OBS noise recordings in the Tuktoyaktuk study area (for position see Figure 2). Although not co-located with one of our H/V measurements with the mobile instrument, the long duration of the OBS deployment allows us to evaluate the

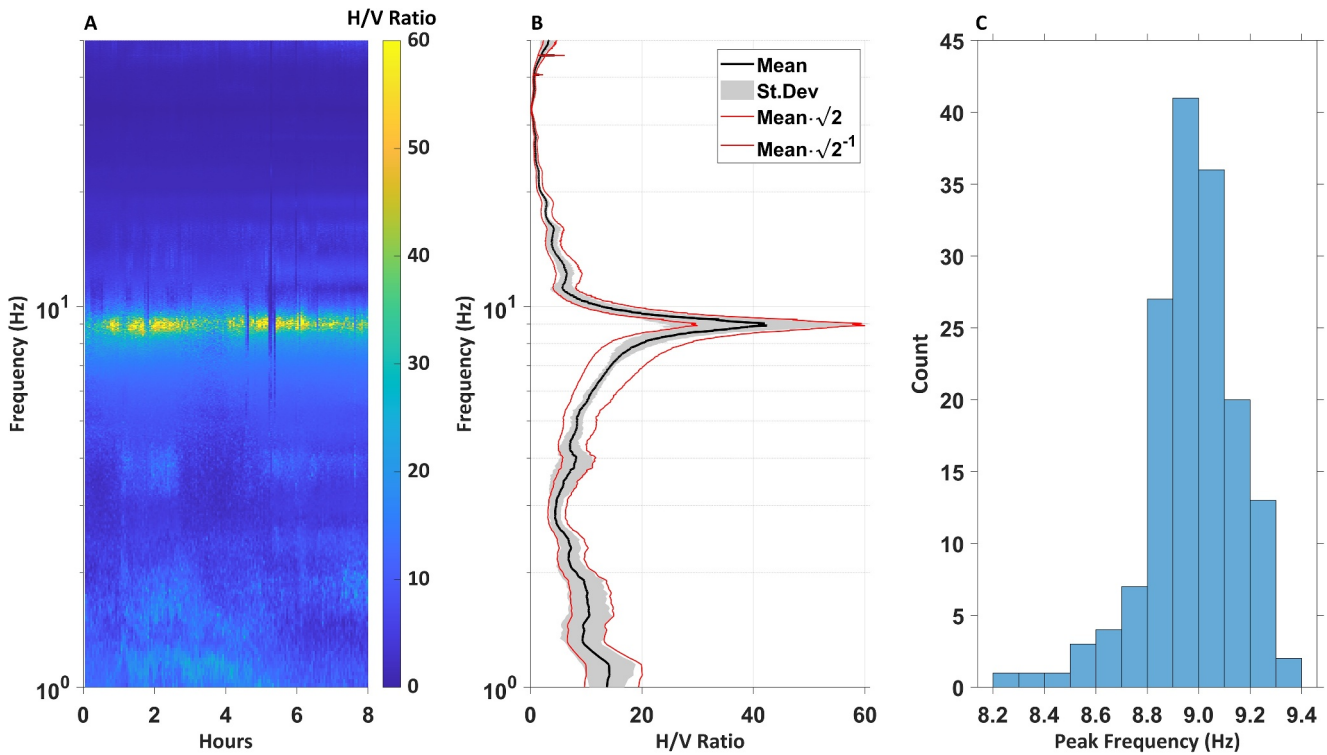


**Figure 5.** An ocean bottom seismometer (OBS) was deployed offshore of Tuktoyaktuk in 2021 (see Figure 2 for position). The temporal evolution of H/V measurements (panel a) illustrate the stability of the peak frequency. Panel (b) displays the mean and standard deviation envelope of the frequency versus H/V ratio. In panel (c), a histogram of the peak frequency is presented.

H/V peak stability and to estimate its uncertainty. The H/V curves determined for sliding windows of 3 min for 8 hr (Figure 5a) show some variability attributed to temporal changes of the seismic noise sources (wind, ocean swells, etc.) including some time windows where no reliable H/V peak determination was possible. In Figure 5b, the mean frequency versus H/V ratio curve is presented along with its standard deviation. Additionally, the mean H/V ratio multiplied by  $\sqrt{2}$  (and its reciprocal) is depicted to illustrate the rationale for employing  $\sqrt{2}$  as a suitable factor in Equation 3 for peak significance. At the same time, the H/V peak frequency related to structures below the ocean bottom, appears to be quite stable; it shows only minor scatter (approximately 0.4 Hz about the mean peak frequency) (Figure 5c). This translates to a peak uncertainty estimate of 5%. The IBPT, as revealed by the shortest path offshore of Tuktoyaktuk, utilizes this uncertainty to assign error bars (refer to Figure 7).

## 5. Discussion

### 5.1. Passive Seismic Determination of Subsea and Sub-Aquatic Permafrost

#### 5.1.1. Sub-Lake Permafrost

Ice-wedge degradation and pond formation around Banja Lake are evident, potentially reflecting recent warming (Figure 1c). Assuming that the degradation of the IBPT beneath Banja Lake initiated recently (less than 100 years ago), the maximum IBPT depths for profiles A-A' and B-B' are plausible. Numerical modeling studies of shallow Siberian thermokarst lakes with a starting water depth of 0.8 m indicate a potential thaw of up to 10 m over 60 years of warming when lateral heat fluxes are considered (Langer et al., 2016). Given Banja Lake's small size, it is conceivable that lateral heat flow slows down talik growth compared to larger water bodies. However, determining the IBPT using the shortest path algorithm beneath small lakes becomes challenging when there is a sedimentary horizon above the IBPT. Take profile A-A', for instance. Two distinct units are evident, with the deeper unit characterized by higher H/V ratios. The shallower peak might signify a contact between unfrozen

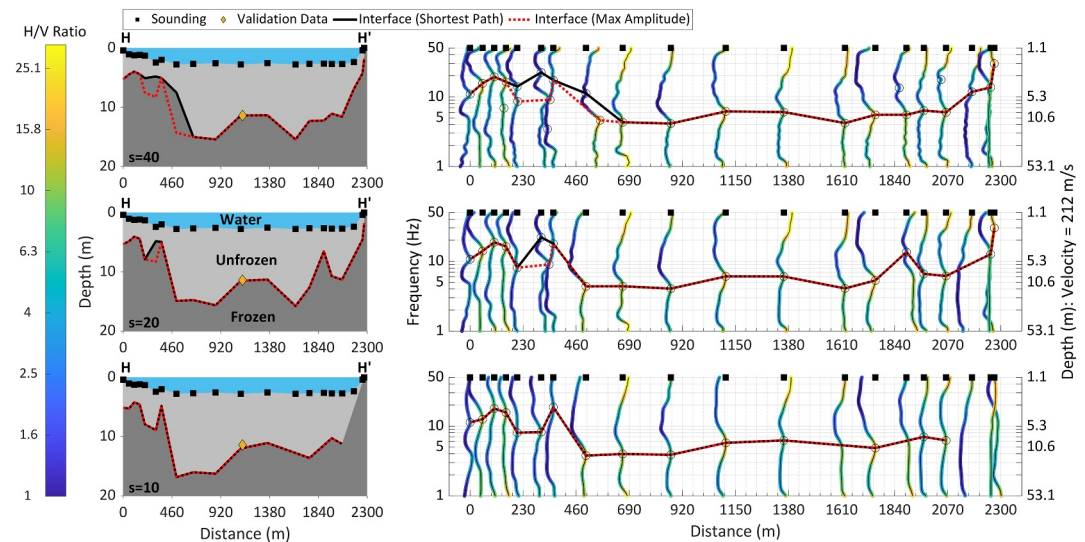


**Figure 6.** Passive seismic findings regarding sub-lagoon permafrost at Ivashkina Lagoon for smoothing parameters of 40 (top), 20 (middle), and 10 (bottom) (Konno & Ohmachi, 1998) applied to the spectra. Refer to the caption in Figure 3 for an explanation of how the H/V measurements are presented and interpreted.

loose lake sediment and thawed permafrost sediment, while the deeper peak represents the IBPT. It is plausible that loose sediment is more pronounced in this setting due to recent thaw settlement.

### 5.1.2. Sub-Lagoon and Subsea Permafrost

Out of all the underwater permafrost classes, MOBSI proves most effective for sub-lagoon and subsea permafrost detection. This efficacy is attributed to several factors. The presence of only one peak candidate for most soundings reduces ambiguity between the shortest path and maximum amplitude-derived interfaces. Furthermore, the homogeneity of the talik contributes to accurate results, with peak frequencies well above the detection limit for the duration of the deployments. At Ivashkina Lagoon, the MOBSI-inferred IBPT varies only between 11 and 15 m bsl over a 1,500 m stretch of the profile (refer to Figure 4). This alignment with borehole observations and the lagoon's thermokarst history reinforces the reliability of the MOBSI method. Notably, since the lagoon is situated within a formerly drained thermokarst lake basin (Schirmeister et al., 2018), the seawater inundation time is uniform throughout the lagoon, except near the thermo-erosional widening shorelines. Offshore of Tuktoyaktuk, there is strong evidence that the peaks represent the IBPT. First, the IBPT is flat along the beach and then gradually deepens with increasing water depth offshore. Since we know the 1947–2022 mean coastal erosion rate, the IBPT is plotted as a function of inundation time in Figure 7. Calibrated by nearshore boreholes offshore of Tuktoyaktuk, these curves are similar to the IBPT degradation rates derived from repeated borehole observations in the Laptev Sea near Muostakh Island (Shakhova et al., 2017). The Mackenzie River near Tuktoyaktuk and the Lena River in Siberia both discharge warm river runoff into the ocean, which enhances the IBPT degradation rate. Therefore, the IBPT depths offshore of Tuktoyaktuk are higher than borehole-derived IBPT depths from the western Laptev Sea (Overduin et al., 2008) and Prudhoe Bay (Alaska) (Osterkamp et al., 1989) for the same inundation period. Top-down salt diffusion and bottom-fast ice are the main mechanisms for the slower degradation rates at these sites (Angelopoulos, Overduin, Miesner, et al., 2020). The only anomaly in the data is farthest offshore peak in Tuktoyaktuk profile G-G' where the IBPT rises at 320 m from the coastline. The most likely explanations are differential thawing rates caused by heterogeneous ground ice volumes or permafrost aggradation phases beneath former spits.

## 5.2. Analysis of H/V Signals

### 5.2.1. H/V Ratio Smoothing

The IBPT profile is influenced by the smoothing factor ( $s$ ) (Konno & Ohmachi, 1998) applied to the H/V ratio curves. The smoothing affects the complexity of the spectra, including the frequency, but more



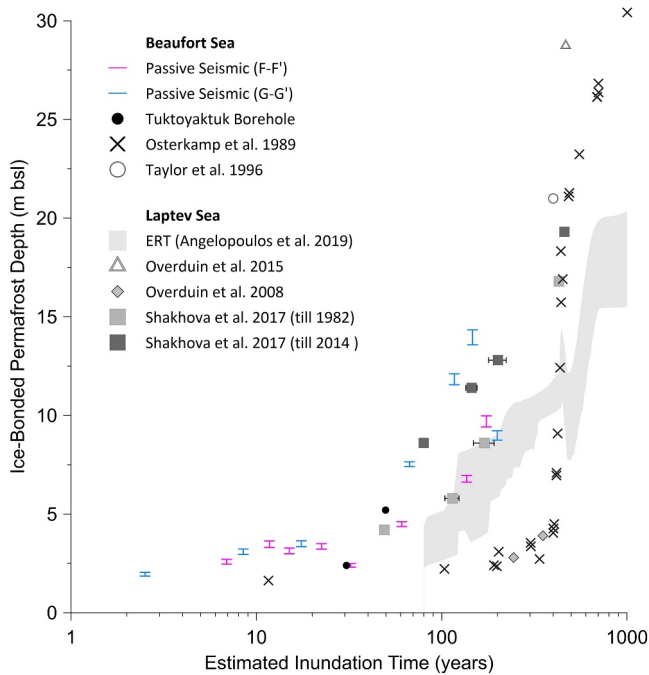


**Figure 7.** The ice-bonded permafrost table (IBPT) depths results obtained from the passive seismic surveys near Tuktoyaktuk Island are plotted against the inundation time derived from the coastal retreat rates published in Whalen et al. (2022). The error bars are derived from the uncertainty estimate of the peak frequency from the ocean bottom seismometer (please refer to Figure 5). To present the data in context, we show IBPT depths from various borehole and electrical resistivity tomography (ERT) studies in the Laptev Sea (Angelopoulos et al. (2019); Overduin et al. (2008); Overduin, Liebner, et al. (2015); Shakhova et al. (2017)), as well as the Canadian and American Beaufort Seas (Osterkamp et al. (1989); Taylor et al. (1996)). Note that Angelopoulos et al. (2019) refer to the ice-bearing permafrost table.

a soft boundary between unfrozen ground and partially frozen saline sediment. Toward the south-easternmost 200 m of the profile, the IBPT is smoothed out completely when a smoothing factor of 10 is applied (Figure 6). Although seasonal sediment freezing can occur beneath the floating ice of saline waters (Osterkamp et al., 1989), the IBPT is probably more gradual (i.e., less abrupt) in this area of Ivashkina Lagoon.

### 5.2.2. Significant Peak Selection

How a significant peak is defined influences the IBPT profiles. The simplest approach is to select one peak per sounding within a specified frequency bandwidth (i.e., the maximum local height or amplitude) assuming that the IBPT is associated with the maximum velocity contrast and H/V ratio peak. This approach has shown to be most effective at Banja Lake, where there appears to be an unfrozen sedimentary horizon above an ice-bonded permafrost table. In subsea environments, however, the shortest path delineates smoother IBPT boundaries. As shown by Overduin, Haberland, et al. (2015), the highest H/V ratio peak is not necessarily the IBPT. Stronger amplitude peaks, but also peaks with relatively high H/V variation (height and frequency) versus time, can be caused by waves and currents. For the soundings presented in our study, the data were collected for only a few to several minutes. While the deployment time is sufficient to observe stable peak frequencies, longer deployment times may provide some information on the temporal H/V variability of other peaks not related to subsurface structures. That is to say, peaks related to subsurface structures typically exhibit less H/V variability over time. Due to our relatively short deployment times, we evaluate peak significance based on peak prominence and the relationship between prominence and height (Equation 3).

importantly, the number of peaks. With smoothing, some of the less prominent peaks are filtered out, as shown in Figure 6 using the IBPT example of Ivashkina Lagoon. This ultimately converges the interface generated with the shortest-path algorithm to that of just picking the maximum amplitude. Though counter-intuitive, increased smoothing results in a more uneven IBPT. This occurs, because the most prominent peaks are now chosen. This results in a sudden IBPT dip (e.g., at 200 m) and steeper IBPT slopes at the profile edges (Figure 6). Since the height of the peak is mostly controlled by the velocity difference between the low velocity and high velocity layer and the intrinsic wave attenuation factor (damping) in the layers (Fäh et al., 2003), the most prominent peak may represent a deeper unfrozen/frozen boundary with a stronger shear wave velocity contrast. In the lagoon center, increased smoothing results in very subtle IBPT changes, because there is only one dominant peak frequency for each sounding between 660 and 1,800 m. Since the sediment temperature regime beneath the lagoon is cryotic (even in the talik) (Schirmermeister et al., 2018; Ulyantsev et al., 2022), the IBPT degradation is controlled by top-down salt flow. The cryotic talik temperatures likely contribute to a faster shear wave velocity (212 m/s) relative to the other sites. The situation beneath bottom-fast ice zones, however, may be quite different. For the north-westernmost 200 m of the profile at Ivashkina Lagoon, all the water depths were 1.3 m or less. Bottom-fast ice presumably covers this entire stretch in winter, resulting in even colder temperature regimes, higher salt concentrations, and a more complex cryostratigraphy relative to the center of the lagoon. Uomullyakh Lagoon, almost 3 km to the west of Ivashkina Lagoon, is very shallow (mean depth of 1 m) and susceptible to widespread bottom-fast ice formation (Jenrich et al., 2021). The bonding of lagoon ice and sediment results in a seasonally frozen saline layer over 1 m thick. Bottom-fast ice at Ivashkina Lagoon may result in similarly alternating unfrozen and frozen sediment states in the cryotic saline permafrost. Hence, the low-height H/V ratio peak at 200 m that is retained under less smoothing ( $s = 40$ ) may represent

Since each sounding is treated individually, the decision about peak significance for one sounding is originally made without any information from neighboring soundings. Since the peak prominence is defined relative to a base level, a small peak has a better chance of qualifying as significant if the base level is low. Since an IBPT-related peak is expected to produce a large H/V ratio ( $>10$ ), selecting low-prominence peaks may lead to a false IBPT detection. Alternative peak selection algorithms calculate global statistics for all peaks for all soundings in an area (Zhu et al., 2021), which may filter out less prominent peaks.

### 5.3. Complementary Geophysics

In sub-aquatic permafrost areas with other significant shear wave velocity contrasts, it is crucial to employ complementary geophysical methods. The Lena River (Chay-Tumus) profile E-E' may exhibit a sediment/bedrock contact (Figure S1), particularly with the presence of an exposed bedrock outcrop along the riverbank (Figure 1d). Given the stability of the Lena River near Chay-Tumus over millennia (Schwamborn et al., 2002), the permafrost table likely lies well beyond the minimum peak frequency detection range of MOBSI. However, in the Lena River profile at Samoylov Island (D-D'), calibration with frost probe measurements likely occurred in a seasonally frozen layer that hadn't fully thawed (Maksimov et al., 2022), leading to merged peaks from unfrozen/frozen boundaries in shallow water (where bottom-fast ice occurs in winter) to other geological boundaries in deeper water (where floating ice occurs in winter) for shortest path and maximum amplitude analyses (Figure S1). Additionally, ERT results from a separate study indicates the sub-aquatic permafrost boundary to be approximately 70 m deep beneath profile D-D' (Juhls et al., 2021). Moving forward, integrating ERT with passive seismic techniques could further enhance the distinction between subsea ice-bearing permafrost and ice-bonded permafrost.

## 6. Conclusions

For deployment times of only a few to several minutes, the MOBSI detected the ice-bonded permafrost table (IBPT) offshore of Tuktoyaktuk in the Canadian Beaufort Sea, beneath Ivashkina Lagoon in the Laptev Sea in Siberia, and below a lake in the Lena Delta in Russia. We applied a shortest path algorithm for H/V peak selection, which allows for IBPT depth determinations assuming a smoothly varying IBPT depth along densely spaced MOBSI profile measurements. We also showed IBPT interfaces as revealed by picking the maximum amplitude. Validated by borehole logs, the IBPT depths near Tuktoyaktuk are among the greatest in the Arctic when plotted as a function of inundation time. Warm discharge water from the Mackenzie River increases the subsea permafrost degradation rate compared to colder marine settings that depend on salt diffusion to thaw the permafrost table. At Ivashkina Lagoon, the bowl-shaped talik is typical for a thermokarst lagoon with thermo-erosional widening of the shorelines. The deepest sections of Banja Lake (i.e., deep enough for floating ice in winter) exhibited two subsurface structures. Since the deeper structure showed higher H/V ratios, it was interpreted to be the IBPT. In shallower lake waters (i.e., where ice is bottom-fast in winter), the chosen peaks closely aligned with the frost probe measurements. Going forward, passive seismology could be effectively combined with other geophysical methods like electrical resistivity tomography (ERT) to enhance subsurface mapping capabilities. Various geophysical techniques have demonstrated their capabilities for subsea and sub-aquatic permafrost mapping, but these studies were often limited to a single method and small spatial extents. With its relatively easy deployment and rapid measurements, passive seismology can bolster two- or three-dimensional ERT to map subsea and sub-aquatic permafrost features.

### Data Availability Statement

The Mobile Ocean Bottom Seismometer Instrument (MOBSI) data presented in this paper are available on the Zenodo data repository (Angelopoulos et al., 2023). Furthermore, a passive seismic data report for Tuktoyaktuk in Canada in 2018 is available from Ryberg et al. (2020). The prolonged offshore measurements, spanning several hours, recorded by the Ocean Bottom Seismometer (OBS) off the coast of Tuktoyaktuk in 2021 are detailed in Ryberg et al. (2022).

### Acknowledgments

This work was supported by funding from the Helmholtz Association in the framework of MOSES (Modular Observation Solutions for Earth Systems). Bennet Juhls was supported by the European Space Agency (ESA) as part of the Climate Change Initiative (CCI) fellowship (ESA ESRIN/Contract No. 4000I3376I/2I/I-NB). We thank Dustin Whalen (Geological Survey of Canada) for his assistance. Open Access funding enabled and organized by Projekt DEAL.

### References

- Acerra, C., Aguacil, G., Anastasiadis, A., Atakan, K., Azzara, R., Bard, P.-Y., et al. (2004). *Guidelines for the implementation of the HV spectral ratio technique on ambient vibrations measurements, processing and interpretation*. European Commission–EVG1-CT-2000-00026 SES-AME. Retrieved from [https://sesame.geopsy.org/Delivrables/Del-D23-HV\\_User\\_Guidelines.pdf](https://sesame.geopsy.org/Delivrables/Del-D23-HV_User_Guidelines.pdf)
- Angelopoulos, M., Overduin, P. P., Jenrich, M., Nitze, I., Günther, F., Strauss, J., et al. (2021). Onshore thermokarst primes subsea permafrost degradation. *Geophysical Research Letters*, *48*(20). <https://doi.org/10.1029/2021gl093881>
- Angelopoulos, M., Overduin, P. P., Miesner, F., Grigoriev, M. N., & Vasiliev, A. A. (2020). Recent advances in the study of Arctic submarine permafrost. *Permafrost and Periglacial Processes*, *31*(3), 442–453. <https://doi.org/10.1002/ppp.2061>
- Angelopoulos, M., Overduin, P. P., Westermann, S., Tronicke, J., Strauss, J., Schirrmeyer, L., et al. (2020). Thermokarst Lake to lagoon transitions in eastern Siberia: Do submerged taliks refreeze? *Journal of Geophysical Research: Earth Surface*, *125*(10). <https://doi.org/10.1029/2019jf005424>
- Angelopoulos, M., Ryberg, T., Rasmussen, C. F., Haberland, C., Juhls, B., Dallimore, S., et al. (2023). Mobile Ocean Bottom Seismometer Instrument (MOBSI) data from Arctic subsea and sub-aquatic permafrost [Dataset]. *Zenodo*. <https://doi.org/10.5281/zenodo.8038782>
- Angelopoulos, M., Westermann, S., Overduin, P., Faguet, A., Olenchenko, V., Grosse, G., & Grigoriev, M. N. (2019). Heat and salt flow in subsea permafrost modeled with CryoGRID2. *Journal of Geophysical Research: Earth Surface*, *124*(4), 920–937. <https://doi.org/10.1029/2018JF004823>
- Arboleda-Zapata, M., Angelopoulos, M., Overduin, P. P., Grosse, G., Jones, B. M., & Tronicke, J. (2022). Exploring the capabilities of electrical resistivity tomography to study subsea permafrost. *The Cryosphere*, *16*(10), 4423–4445. <https://doi.org/10.5194/tc-16-4423-2022>
- Are, F., & Reimnitz, E. (2000). An overview of the Lena River delta setting: Geology, tectonics, geomorphology, and hydrology. *Journal of Coastal Research*, *16*(4), 1083–1093. Retrieved from <https://www.jstor.org/stable/4300125>
- Blackwell, S. B., Nations, C. S., McDonald, T. L., Thode, A. M., Mathias, D., Kim, K. H., et al. (2015). Effects of airgun sounds on bowhead whale calling rates: Evidence for two behavioral thresholds. *PLoS One*, *10*(6), e0125720. <https://doi.org/10.1371/journal.pone.0125720>
- Boike, J., & Dallimore, S. R. (2019). Summary of 2018 Mackenzie Delta permafrost field campaign (mCAN2018), Northwest Territories (Tech. Rep. No. 8640). <https://doi.org/10.4095/315704>
- Boike, J., Georgi, C., Kirilin, G., Muster, S., Abramova, K., Fedorova, I., et al. (2015). Thermal processes of thermokarst lakes in the continuous permafrost zone of northern Siberia—Observations and modeling (Lena River Delta, Siberia). *Biogeosciences*, *12*(20), 5941–5965. <https://doi.org/10.5194/bg-12-5941-2015>
- Boike, J., Veh, G., Piel, K., Stof, G., & Muster, S. (2015). Orthomosaic of Samoylov island, Siberia, summer 2006 (382 MB) [Dataset]. *PANGAEA*. <https://doi.org/10.1594/PANGAEA.845722>
- Brothers, L. L., Herman, B. M., Hart, P. E., & Ruppel, C. D. (2016). Subsea ice-bearing permafrost on the US Beaufort Margin: 1. Minimum seaward extent defined from multichannel seismic reflection data. *Geochemistry, Geophysics, Geosystems*, *17*(11), 4354–4365. <https://doi.org/10.1002/2016GC006584>
- Cheng, F., Lindsey, N. J., Sobolevskaia, V., Dou, S., Freifeld, B., Wood, T., et al. (2022). Watching the cryosphere thaw: Seismic monitoring of permafrost degradation using distributed acoustic sensing during a controlled heating experiment. *Geophysical Research Letters*, *49*(10), e2021GL097195. <https://doi.org/10.1029/2021GL097195>
- Chetverova, A., Skorospekhova, T., Morgenstern, A., Alekseeva, N., Spiridonov, I., & Fedorova, I. (2018). Hydrological and hydrochemical characteristics of lakes in the Lena River delta (Northeast-Siberia, Russia). *Polarforschung*. <https://doi.org/10.2312/POLARFORSCHUNG.87.2.111>
- Duchesne, M. J., Fabien-Ouellet, G., & Bustamante, J. (2023). Detecting subsea permafrost layers on marine seismic data: An appraisal from forward modelling. *Near Surface Geophysics*, *21*(1), 3–20. <https://doi.org/10.1002/msg.12231>
- Fäh, D., Kind, F., & Giardini, D. (2003). S-wave velocity structures from average HV ratios, and their use for the estimation of site-effects. *Journal of Seismology*, *7*(4), 449–467. <https://doi.org/10.1023/B:JOSE.0000005712.86058.42>
- Grob, H., Riedel, M., Duchesne, M., Krastel, S., Bustamante, J., Fabien-Ouellet, G., et al. (2023). Revealing the extent of submarine permafrost and gas hydrates in the Canadian Arctic Beaufort Sea using seismic reflection indicators. *Geochemistry, Geophysics, Geosystems*, *24*(5), e2023GC010884. <https://doi.org/10.1029/2023GC010884>
- Grosse, G., Romanovsky, V., Walter, K., Morgenstern, A., Lantuit, H., & Zimov, S. (2008). Distribution of thermokarst lakes and ponds at three yedoma sites in Siberia. In D. Kane & K. Hinkel (Eds.), *Proceedings: Ninth International Conference on Permafrost* (pp. 551–556). Retrieved from <https://epic.awi.de/id/eprint/19086/>
- Grosse, G., Schirrmeyer, L., Kunitsky, V. V., & Hubberten, H.-W. (2005). The use of CORONA images in remote sensing of periglacial geomorphology: An illustration from the NE Siberian coast. *Permafrost and Periglacial Processes*, *16*(2), 163–172. <https://doi.org/10.1002/ppp.509>
- Grosse, G., Schirrmeyer, L., Siegert, C., Kunitsky, V. V., Slagoda, E. A., Andreev, A. A., & Dereviagny, A. Y. (2007). Geological and geomorphological evolution of a sedimentary periglacial landscape in Northeast Siberia during the Late Quaternary. *Geomorphology*, *86*(1–2), 25–51. <https://doi.org/10.1016/j.geomorph.2006.08.005>
- Günther, F., Overduin, P. P., Yakshina, I. A., Opel, T., Baranskaya, A. V., & Grigoriev, M. N. (2015). Observing Muostakh disappear: Permafrost thaw subsidence and erosion of a ground-ice-rich island in response to arctic summer warming and sea ice reduction. *The Cryosphere*, *28*(1), 151–178. <https://doi.org/10.5194/tc-9-151-2015>
- Hauck, C. (2013). New concepts in geophysical surveying and data interpretation for permafrost terrain. *Permafrost and Periglacial Processes*, *24*(2), 131–137. <https://doi.org/10.1002/ppp.1774>
- Hu, K., Issler, D., Chen, Z., & Brent, T. (2013). Permafrost investigation by well logs, and seismic velocity and repeated shallow temperature surveys, Beaufort-Mackenzie Basin Open File Rep. *The Geological Survey of Canada*, 6956, 228. <https://doi.org/10.4095/293120>
- Ibs-von Seht, M., & Wohlenberg, J. (1999). Microtremor measurements used to map thickness of soft sediments. *Bulletin of the Seismological Society of America*, *89*(1), 250–259. <https://doi.org/10.1785/BSSA0890010250>
- Jenrich, M., Angelopoulos, M., Grosse, G., Overduin, P. P., Schirrmeyer, L., Nitze, I., et al. (2021). Thermokarst lagoons: A core-based assessment of depositional characteristics and an estimate of carbon pools on the Bykovsky Peninsula. *Frontiers in Earth Science*, *9*. <https://doi.org/10.3389/feart.2021.637899>
- Juhls, B., Antonova, S., Angelopoulos, M., Bobrov, N., Grigoriev, M., Langer, M., et al. (2021). Serpentine (floating) ice channels and their interaction with riverbed permafrost in the Lena River Delta, Russia. *Frontiers in Earth Science*, *9*, 689941. <https://doi.org/10.3389/feart.2021.689941>
- Köhler, A., & Weidle, C. (2019). Potentials and pitfalls of permafrost active layer monitoring using the HVSR method: A case study in Svalbard. *Earth Surface Dynamics*, *7*(1), 1–16. <https://doi.org/10.5194/esurf-7-1-2019>



- Konno, K., & Ohmachi, T. (1998). Ground-motion characteristics estimated from spectral ratio between horizontal and vertical components of microtremor. *Bulletin of the Seismological Society of America*, 88(1), 228–241. <https://doi.org/10.1785/BSSA0880010228>
- Krylov, A. A., Kulikov, M. E., Kovachev, S. A., Medvedev, I. P., Lobkovsky, L. I., & Semiletov, I. P. (2022). Peculiarities of the HVSR method application to seismic records obtained by ocean-bottom seismographs in the Arctic. *Applied Sciences*, 12(19), 9576. <https://doi.org/10.3390/app12199576>
- Kula, D., Olszewska, D., Dobiński, W., & Glazer, M. (2018). Horizontal-to-vertical spectral ratio variability in the presence of permafrost. *Geophysical Journal International*, 214(1), 219–231. <https://doi.org/10.1093/gji/ggy118>
- Kurfurst, P., & Dallimore, S. (1991). Engineering geology of nearshore areas off Richards Island, NWT: A comparison of stable and actively eroding coastlines. *Canadian Geotechnical Journal*, 28(2), 179–188. <https://doi.org/10.1139/t91-025>
- Langer, M., Westermann, S., Boike, J., Kirillin, G., Grosse, G., Peng, S., & Krinner, G. (2016). Rapid degradation of permafrost underneath waterbodies in tundra landscapes—Toward a representation of thermokarst in land surface models. *Journal of Geophysical Research: Earth Surface*, 121(12), 2446–2470. <https://doi.org/10.1002/2016JF003956>
- Lendl, C. (2021). *GIPPTools*. Zenodo. <https://doi.org/10.5281/zenodo.4972595>
- Loke, M., & Lane, J. W., Jr. (2004). Inversion of data from electrical resistivity imaging surveys in water-covered areas. *Exploration Geophysics*, 35(4), 266–271. <https://doi.org/10.1071/EG04266>
- Lunedei, E., & Malischewsky, P. (2015). A review and some new issues on the theory of the H/V technique for ambient vibrations. In *Perspectives on European earthquake engineering and seismology* (Vol. 2, pp. 371–394). <https://doi.org/10.1007/978-3-319-16964-4>
- Maksimov, G., Grigoriev, M., & Bolshiyarov, D. (2022). Formation and distribution of permafrost and taliks under the channels of the channel in the delta of the Lena River. *Natural Resources of the Arctic and Subarctic*, 27(3), 370–380. <https://doi.org/10.31242/2618-9712-2022-27-3-370-380>
- McCauley, R. D., Day, R. D., Swadling, K. M., Fitzgibbon, Q. P., Watson, R. A., & Semmens, J. M. (2017). Widely used marine seismic survey air gun operations negatively impact zooplankton. *Nature Ecology & Evolution*, 1(7), 0195. <https://doi.org/10.1038/s41559-017-0195>
- Miesner, F., Overduin, P., Grosse, G., Strauss, J., Langer, M., Westermann, S., et al. (2023). Subsea permafrost organic carbon stocks are large and of dominantly low reactivity. *Scientific Reports*, 13(1), 9425. <https://doi.org/10.1038/s41598-023-36471-z>
- Morgenstern, A., Meyer, H., Overduin, P. P., Blender, F., Bolshiyarov, D. Y., & Grigoriev, M. N. (2017). *Russian-German cooperation: Expeditions to Siberia in 2016* (Tech. Rep.). Alfred-Wegener-Institut, Helmholtz-Zentrum für Polar- und Meeresforschung. [https://doi.org/10.2312/BZPM\\_0709\\_2017](https://doi.org/10.2312/BZPM_0709_2017)
- Murton, J. B. (2001). Thermokarst sediments and sedimentary structures, Tuktoyaktuk Coastlands, western Arctic Canada. *Global and Planetary Change*, 28(1–4), 18. [https://doi.org/10.1016/S0921-8181\(00\)00072-2](https://doi.org/10.1016/S0921-8181(00)00072-2)
- Osterkamp, T., Baker, G., Harrison, W., & Matava, T. (1989). Characteristics of the active layer and shallow subsea permafrost. *Journal of Geophysical Research*, 94(C11), 16227–16236. <https://doi.org/10.1029/JC094iC11p16227>
- Overduin, P. P., Haberland, C., Ryberg, T., Kneier, F., Jacobi, T., Grigoriev, M. N., & Ohrnberger, M. (2015). Submarine permafrost depth from ambient seismic noise. *Geophysical Research Letters*, 42(18), 7581–7588. <https://doi.org/10.1002/2015GL065409>
- Overduin, P. P., Liebner, S., Knoblauch, C., Günther, F., Wetterich, S., Schirmeister, L., et al. (2015). Methane oxidation following submarine permafrost degradation: Measurements from a central Laptev Sea shelf borehole. *Journal of Geophysical Research: Biogeosciences*, 120(5), 965–978. <https://doi.org/10.1002/2014JG002862>
- Overduin, P. P., Rachold, V., & Grigoriev, M. N. (2008). The state of subsea permafrost in the Western Laptev nearshore zone. In D. L. Kane & K. M. Hinkel (Eds.), *Proceedings: Ninth International Conference on Permafrost* (Vol. 2, pp. 1345–1350).
- Overduin, P. P., Schneider von Deimling, T., Miesner, F., Grigoriev, M., Ruppel, C., Vasiliev, A., et al. (2019). Submarine permafrost map in the Arctic modeled using 1-D transient heat flux (SuPerMAP). *Journal of Geophysical Research: Oceans*, 124(6), 3490–3507. <https://doi.org/10.1029/2018JC014675>
- Overduin, P. P., Westermann, S., Yoshikawa, K., Haberland, T., Romanovsky, V., & Wetterich, S. (2012). Geoelectric observations of the degradation of nearshore submarine permafrost at Barrow (Alaskan Beaufort Sea). *Journal of Geophysical Research*, 117(F2). <https://doi.org/10.1029/2011JF002088>
- Pedrazas, M. N., Cardenas, M. B., Demir, C., Watson, J. A., Connolly, C. T., & McClelland, J. W. (2020). Absence of ice-bonded permafrost beneath an Arctic lagoon revealed by electrical geophysics. *Science Advances*, 6(43), eabb5083. <https://doi.org/10.1126/sciadv.abb5083>
- Pontrelli, M. A. (2019). Assessing site response complexity using single station HVSR: Mexico City case study. Retrieved from [https://sites.tufts.edu/geohazards/files/2020/12/Pontrelli\\_Thesis\\_Final1.pdf](https://sites.tufts.edu/geohazards/files/2020/12/Pontrelli_Thesis_Final1.pdf)
- Rekant, P., & Vasiliev, A. (2011). Distribution of subsea permafrost at the Kara Sea shelf. *Cryosphere of the Earth*, 4, 69–72.
- Riedel, M., Brent, T., Taylor, G., Taylor, A., Hong, J.-K., Jin, Y.-K., & Dallimore, S. (2017). Evidence for gas hydrate occurrences in the Canadian Arctic Beaufort Sea within permafrost-associated shelf and deep-water marine environments. *Marine and Petroleum Geology*, 81, 66–78. <https://doi.org/10.1016/j.marpetgeo.2016.12.027>
- Ruppel, C. D. (2015). Permafrost-associated gas hydrate: Is it really approximately 1% of the global system? *Journal of Chemical and Engineering Data*, 60(2), 429–436. <https://doi.org/10.1021/je500770m>
- Ruppel, C. D., & Kessler, J. D. (2017). The interaction of climate change and methane hydrates: Climate-Hydrates Interactions. *Reviews of Geophysics*, 55(1), 126–168. <https://doi.org/10.1002/2016RG000534>
- Ryberg, T., Cable, W., Overduin, P., & Haberland, C. (2020). Ambient seismic noise data from the shallow sea floor off Tuktoyaktuk, Canada [Dataset]. <https://doi.org/10.5880/GIPP.201899.1>
- Ryberg, T., Haberland, C., Overduin, P., & Cable, W. (2022). Subaquatic ambient seismic noise recordings acquired in the region of Inuvik and Tuktoyaktuk, Northwest Territories, Canada [Dataset]. <https://doi.org/10.5880/GIPP.202199.1>
- Sapart, C. J., Shakhova, N., Semiletov, I., Jansen, J., Szidat, S., Kosmach, D., et al. (2017). The origin of methane in the East Siberian Arctic Shelf unraveled with triple isotope analysis. *Biogeosciences*, 14(9), 2283–2292. <https://doi.org/10.5194/bg-14-2283-2017>
- Schirmeister, L., Grigoriev, M. N., Strauss, J., Grosse, G., Overduin, P. P., Kholodov, A., et al. (2018). Sediment characteristics of a thermokarst lagoon in the northeastern Siberian Arctic (Ivashkina Lagoon, Bykovsky Peninsula). *Arktos*, 4(1), 13–16. <https://doi.org/10.1007/s41063-018-0049-8>
- Schirmeister, L., Grosse, G., Schwamborn, G., Andreev, A. A., Meyer, H., Kunitsky, V. V., et al. (2003). Late Quaternary history of the accumulation plain north of the Chekanovsky Ridge (Lena Delta, Russia): A multidisciplinary approach. *Polar Geography*, 27(4), 277–319. <https://doi.org/10.1080/0789610225>
- Schwamborn, G., Dix, J. K., Bull, J. M., & Rachold, V. (2002). High-resolution seismic and ground penetrating radar-geophysical profiling of a thermokarst lake in the western Lena Delta, Northern Siberia. *Permafrost and Periglacial Processes*, 13(4), 259–269. <https://doi.org/10.1002/ppp.430>

- Scott, W., Sellmann, P., & Hunter, J. (1978). Geophysics in the study of permafrost. In W. J. Scott, P. V. Sellmann, & J. A. Hunter (Eds.), *Proceedings. Society of Exploration Geophysicists*. <https://doi.org/10.1190/1.9781560802785>
- Shakhova, N., Semiletov, I., Gustafsson, O., Sergienko, V., Lobkovsky, L., Dudarev, O., et al. (2017). Current rates and mechanisms of subsea permafrost degradation in the East Siberian Arctic Shelf. *Nature Communications*, 8(1), 15872. <https://doi.org/10.1038/ncomms15872>
- Sherman, D., Kannberg, P., & Constable, S. (2017). Surface towed electromagnetic system for mapping of subsea Arctic permafrost. *Earth and Planetary Science Letters*, 460, 97–104. <https://doi.org/10.1016/j.epsl.2016.12.002>
- Siegert, C., Schirrmeister, L., & Babiy, O. (2002). The sedimentological, mineralogical and geochemical composition of Late Pleistocene deposits from the Ice complex on the Bykovsky Peninsula, Northern Siberia. *Polarforschung*, 70, 3–11. Retrieved from <https://epic.awi.de/id/eprint/5129/>
- Stevens, C. W., Moorman, B. J., Solomon, S. M., & Hugenholtz, C. H. (2009). Mapping subsurface conditions within the near-shore zone of an Arctic delta using ground penetrating radar. *Cold Regions Science and Technology*, 56(1), 30–38. <https://doi.org/10.1016/j.coldregions.2008.09.005>
- Stocker, T. F., Qin, D., Plattner, G.-K., Tignor, M. M., Allen, S. K., Boschung, J., et al. (2014). *Climate Change 2013: The Physical Science Basis. Contribution of Working Group I to the Fifth Assessment Report of IPCC the Intergovernmental Panel on Climate Change*. Cambridge University Press.
- Taylor, A. E., Dallimore, S., Hill, P., Issler, D., Blasco, S., & Wright, F. (2013). Numerical model of the geothermal regime on the Beaufort shelf, Arctic Canada since the last interglacial. *Journal of Geophysical Research: Earth Surface*, 118(4), 2365–2379. <https://doi.org/10.1002/2013JF002859>
- Taylor, A. E., Dallimore, S. R., & Outcalt, S. I. (1996). Late Quaternary history of the Mackenzie–Beaufort region, Arctic Canada, from modelling of permafrost temperatures. 2. The onshore-offshore transition. *Canadian Journal of Earth Sciences*, 33(1), 52–61. <https://doi.org/10.1139/e96-006>
- Ulyantsev, A., Bratskaya, S. Y., Romankevich, E., Semiletov, I., & Avramenko, V. (2016). Particle size composition of Holocene–Pleistocene deposits of the Laptev Sea (Buor-Khaya Bay). *Doklady Earth Sciences*, 467(1), 241–245. <https://doi.org/10.1134/S1028334X16030168>
- Ulyantsev, A., Polyakova, N., Trukhin, I., Parotkina, Y., Dudarev, O., & Semiletov, I. (2022). Peculiarities of pore water ionic composition in the bottom sediments and subsea permafrost: A case study in the Buor-Khaya Bay. *Geosciences*, 12(2), 49. <https://doi.org/10.3390/geosciences12020049>
- Whalen, D., Forbes, D. L., Kostylev, V., Lim, M., Fraser, P., Nedimović, M. R., & Stuckey, S. (2022). Mechanisms, volumetric assessment, and prognosis for rapid coastal erosion of Tuktoyaktuk Island, an important natural barrier for the harbour and community. *Canadian Journal of Earth Sciences*, 59(11), 945–960. <https://doi.org/10.1139/cjes-2021-0101>
- Wolfe, S., Dallimore, S., & Solomon, S. (1998). Coastal permafrost investigations along a rapidly eroding shoreline, Tuktoyaktuk, NWT. In *Proceedings: Seventh International Conference on Permafrost* (pp. 1125–1131).
- Zhu, C., Weatherill, G., Cotton, F., Pilz, M., Kwak, D. Y., & Kawase, H. (2021). An open-source site database of strong-motion stations in Japan: K-Net and kik-net (v1. 0.0). *Earthquake Spectra*, 37(3), 2126–2149. <https://doi.org/10.1177/8755293020988028>